Poking and bulging of suspended thin sheets: Slippage, instabilities, and metrology

Zhaohe Dai [*], Nanshu Lu [*]

Center for Mechanics of Solids, Structures and Materials, Department of Aerospace Engineering and Engineering Mechanics, The University of Texas at Austin, Austin, Texas 78712, USA

ARTICLE INFO

ABSTRACT

Measurement of in-plane elasticity of thin sheets often leverages out-of-plane poking or bulging, also known as indentation or bulge tests. For linear elastic sheets, a load-cubic deflection relation has been frequently assumed so that the stiffness of the sheet could be readily extracted. However, we find that recent results of indentation and bulge tests on 2D materials do not support the assumption, which can be attributed to the slippage of 2D materials against their supporting substrates. Besides, the interfacial slippage could cause instabilities in the sheet such as radial wrinkles in suspended region, with finite lengths. To gain a quantitative understanding, we assume constant interfacial shear traction and study the wrinkling extent and the effective stiffness of thin sheets upon poking and bulging. We identify a single dimensionless parameter governing these mechanical responses—the sliding number—defined by comparing the sheet tension (that drives the slippage) with the interfacial traction (that resists the slippage). We discuss several useful asymptotic behaviors emerging at small and large sliding numbers. These understandings inspire when the effect of the interfacial slippage (as well as other substrate-associated subtleties) can be neglected in these tests. For instance, traditional bulge and indentation tests suffer from complexities caused by the slippage, pretension, Poisson's ratio, substrate roughness, and various interfacial traction-separation laws. Based on such understandings, we propose a simple poking/ bulging methodology immune to all of these complexities, enabling an alternative way to measure the sheet stiffness.

1. Introduction

Indentation and bulge tests are popular methods for measuring the mechanical properties of thin sheets because of their ease of specimen mounting and loading. They have been widely used for detecting the pretension and Young's modulus of metallic, polymeric, and biological membranes (Cao et al., 2016; Chen et al., 2018; Diab et al., 2020; Vlassak and Nix, 1992) as well as emerging atomically thin 2D materials (Koenig et al., 2011; Novoselov et al., 2016). To carry out such experiments, a transverse force or a pressure is carefully applied to the thin sheet, and the resulted deflection is precisely measured, yielding the load-deflection curve. The interpretation of the load-deflection curve, however, is a nontrivial task even for linear elastic isotropic thin sheets due to the inherent nonlinearity of the deformed geometry (Chandler and Vella, 2020; Jia and Amar, 2020). The task would be further complicated by the

* Corresponding authors at: Center for Mechanics of Solids, Structures and Materials, Department of Aerospace Engineering and Engineering Mechanics, The University of Texas at Austin, Austin, Texas 78712, USA.
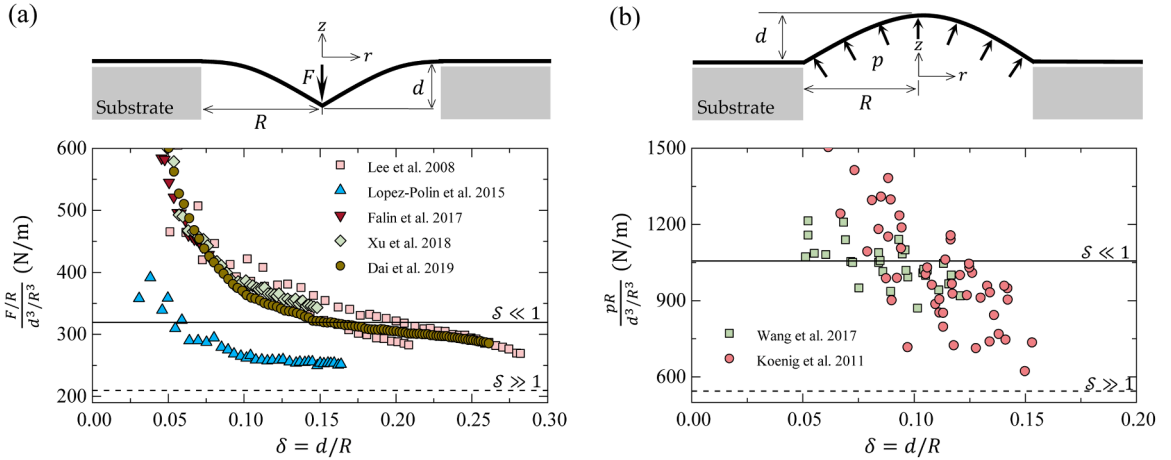*E-mail addresses:* daizh@utexas.edu (Z. Dai), nanshulu@utexas.edu (N. Lu).

Fig. 1. (a) A schematic of the indentation test and the rescaled indentation force-deflection relations measured on monolayer graphene extracted from multiple publications (Dai *et al.*, 2019; Falin *et al.*, 2017; Lee *et al.*, 2008; López-Polín *et al.*, 2015; Xu *et al.*, 2018). (b) A schematic of the bulge test and the rescaled pressure-deflection relations measured on monolayer graphene (Koenig *et al.*, 2011; Wang *et al.*, 2017). The solid lines are theoretical results assuming pretension-free sheets supported by clamped interfaces (i.e., the strong-shear limit of Case I discussed in Section 4). The dashed lines are theoretical results assuming pretension-free sheets supported by lubricated interfaces (i.e., the weak-shear limit of Case II in Section 4);.

pretension in the sheet that could be induced by sheet growth or transfer.

A simplified force-deflection relationship for the indentation test has been widely adopted in the literature (particularly when analyzing the indentation of 2D materials). It embodies asymptotic solutions at the small and large deformation of a thin circular sheet of radius R, stiffness E_{2D}, and pretension t_{pre} (Lee *et al.*, 2008),

$$F = \pi t_{pre}d + \alpha_{\mathcal{F}}(\nu)\frac{E_{2D}}{R^2}d^3, \tag{1.1}$$

where d is the center deflection, ν is the Poisson's ratio of the sheet, and $\alpha_{\mathcal{F}}(\nu) = (1.0491 - 0.1462\nu - 0.15827\nu^2)^{-3}$.

Much predating the indentation technique, bulge test was first introduced to measure the mechanical properties of thin sheets by Beams in 1959 (Beams, 1959). A number of researchers have examined the validity and accuracy of this method. For example, Itozaki reported an important role played by the initial sheet height in the mechanical response (Itozaki, 1982). Using finite element methods, Small and Nix analyzed the effect of initial film conditions, including the initial height, wrinkles, and residual stresses (Small and Nix, 1992). Neglecting the bending stiffness of thin sheets, Hencky gave an analytical solution in the form of power series for the pressure-deflection relation of a circular membrane with fixed edges (Hencky, 1915). Vlassak further considered the contribution of residual stress to such pressure-deflection relation (Vlassak, 1994). Here, we modify Vlassak's expression slightly by using a different prefactor for the nonlinear term,

$$p = \frac{4t_{pre}}{R^2}d + \alpha_P(\nu)\frac{E_{2D}}{R^4}d^3, \tag{1.2}$$

where $\alpha_P(\nu) = (0.7179 - 0.1706\nu - 0.1495\nu^2)^{-3}$. We adopt the prefactors, $\alpha_{\mathcal{F}}(\nu)$ and $\alpha_P(\nu)$, from numerical calculations of pretension-free sheets under clamped boundary conditions (Komaragiri *et al.*, 2005).

Following conventional analysis of thin film bulge tests, state-of-the-art practice for 2D materials is to use (1.1) to fit measured force-deflection data and obtain the pretension and the stiffness of the sheet as fitting parameters (Lee *et al.*, 2008). In bulge tests of 2D materials, however, the pretension term in (1.2) is often neglected, and the cubic term is used to determine the stiffness of the sheet (Koenig *et al.*, 2011). The simplicity of the two formulae enables a quick interpretation of the measured load-deflection data but could produce significant errors. For (1.1), the linear term does not involve a length scale for the indenter size, challenging the validity of the fitted pretension (Vella and Davidovitch, 2017). Besides, the summation of asymptotic solutions for small (the linear term dominates) and large (the cubic term dominates) deformation fails to describe the transition regime between the two. Specifically, the deviation from calculation increases with decreasing indenter size and can be up to 60% (Vella and Davidovitch, 2017). The deviation associated with (1.2) is less than 2%. However, omitting the linear term in previous bulge test interpretations not only precludes the estimation of the pretension but also introduces noticeable errors for the extracted in-plane stiffness if the pressurization is within the transition regime.

These issues become insignificant when the pressurized or indented deflection is so large that the cubic term dominates the mechanical response of the sheet. The question is whether the deflection has been appropriate in previous experiments of 2D materials that were analyzed by (1.1) or (1.2). We answer this question by re-plotting load-deflection relations measured from monolayer graphene in the following section. The paper outline will be offered at the end of Section 2.
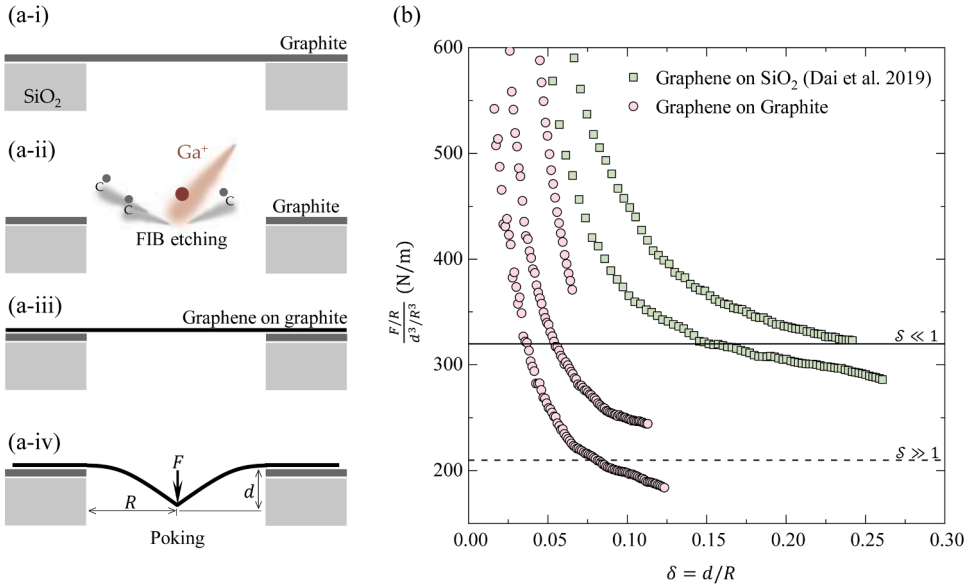
Fig. 2. (a) Schematics of the fabrication and indentation of monolayer graphene supported by a graphite substrate. (b) Rescaled indentation force-deflection relations measured on SiO$_2$-supported (green squares) and graphite-supported (pink circles) monolayer graphene. The experimental setting follows (Dai et al., 2019). A slight difference is that the drumhead radius is 0.5 μm for graphene on SiO$_2$ and 2.5 μm for graphene on graphite because the 2.5-μm-radius holes are easier to etch by focused ion beam (FIB) illustrated in (a-ii). The graphite-supported graphene results could even drop below the weak-shear limit, possibly due to the finite size of the sheet that is smaller than the sliding extent.

2. Experiments

2.1. Previous load-deflection data

A variety of atomically thin 2D materials have been fabricated recently (Novoselov et al., 2016). Due to their perfectly crystalline structures, they typically possess outstanding elastic properties, which, for the most part, are measured by the indentation tests (Akinwande et al., 2017). Monolayer graphene is the first mechanically tested 2D material. Fitting the indentation result with (1.1) leads to an in-plane stiffness of ~340 N/m, amounting to Young's modulus of ~1 TPa if taking the sheet thickness to be the interlayer spacing in bulk graphite (0.335 nm) (Lee et al., 2008). This value agrees well with that obtained through fitting the bulge test with (1.2) later (Koenig et al., 2011) as well as first-principles calculations (Kudin et al., 2001; Wei et al., 2009).

A number of reports on the indentation of pristine monolayer graphene are available in the literature, and they serve as a benchmark against which graphene derivatives and other 2D materials could compare (Dai et al., 2019; Falin et al., 2017; Lee et al., 2008; López-Polín et al., 2015; Xu et al., 2018).

In Fig. 1a, we plot these results using the rescaled force FR^2/d^3 vs. deflection d/R. In this way, the coefficient in front of d^3/R^2 in (1.1), $\alpha_{\mathcal{F}}(\nu)E_{2D}$, is simply a horizontal solid line in Fig. 1a, which is determined using the following well-accepted values for graphene: $\nu = 0.165$ and $E_{2D} = 340$ N/m. It is obvious in this plot that the experimental results rarely agree with the force-cubic deflection relation. Instead, the experimentally measured rescaled force keeps decreasing with increasing indentation depth. It is even surprising to notice that the experimental results can fall through the horizontal solid line as d/R increases. This suggests that instead of being in the transition regime, the deformation in previous experiments might be beyond the linear to cubic transition. In fact, the deformation turns out to be so large that certain softening mechanisms get triggered, which invalidate the $F \sim d^3$ relation. This discovery holds for indentation experiments on other monolayer 2D materials, including Mxene, WS$_2$, MoS$_2$, hBN, and Perovskite (Appendix A). Similar behavior is also observed in the bulge test of monolayer graphene (Fig. 1b), in which we rescale the applied pressure by pR^4/d^3 and the horizontal solid line represents $\alpha_p(\nu)E_{2D}$, the coefficient in front of d^3/R^4 in (1.2) (Koenig et al., 2011; Wang et al., 2017).

Is this softening a material or structural behavior? *Ab initio* calculations of monolayer graphene have revealed that nonlinear elasticity initiates at ~5% strain, and anisotropy becomes noticeable at ~15% strain (Wei et al., 2009). In Fig. 1, the sheets typically start to soften before $d/R = 0.2$, at which the strain level is ~4% such that most area of the sheet can still be considered isotropic and linearly elastic. Herein, we suggest that the breakdown of $F \sim d^3$ and $p \sim d^3$ relations stem from the relaxation of the clamped boundary condition: when subjected to large enough transverse loads, the sheet would slide on its substrate radially inward. In fact, sliding has been a longstanding hurdle for the indentation and bulge tests of thin sheets because it is challenging to perfectly glue or fix a thin sheet to its substrate. The problem would be exacerbated when the sheet is of atomic thinness and smoothness. Previous indentation and bulge tests on 2D materials usually suspend the sheet over a substrate with pre-patterned holes and simply rely on the spontaneous van der Waals (vdW) interaction between the 2D material and the supporting substrate as fixture. However, vdW interfaces are known to be weak in resisting tangential separations (Dai et al., 2016; Gong et al., 2010; Jiang et al., 2014).
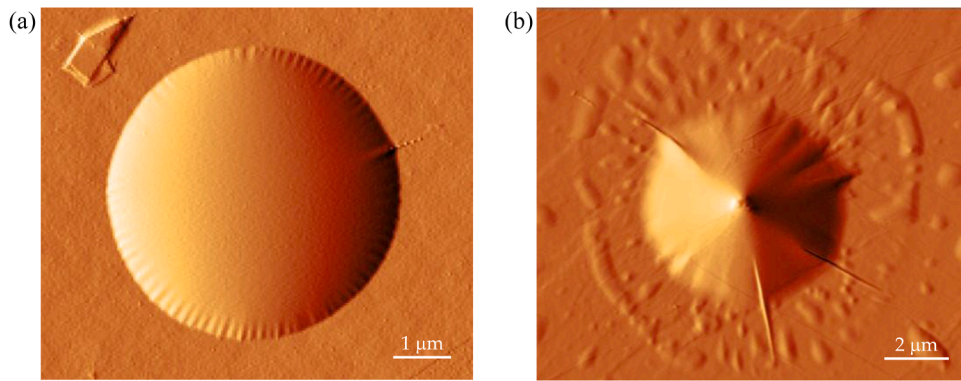
Fig. 3. Atomic force microscopic (AFM) amplitude images of a gas-pressurized bilayer graphene bubble (a) (Wang *et al.*, 2017) and a multilayer graphene tent (b) (Dai *et al.*, 2020b).
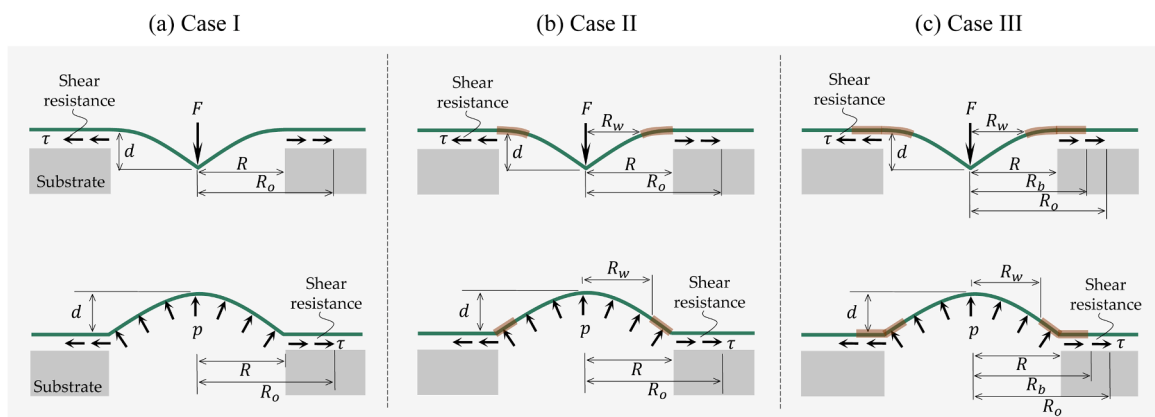
Fig. 4. (a-c) Schematics for three possible deformed configurations when the sheet is allowed to slide against its supporting substrate in the indentation (top) and bulge (bottom) tests. All lengths labeled in the figure are normalized by the radius of the hole *R*. ρ_o represents the normalized outer radius of the sliding zone (i.e., the sliding extent). The brown-shaded part of the sheet denotes the region with instability.

2.2. Poking on sheets with lubricated interfaces

To further clarify the sliding effect, we compare indentation tests with intentionally designed strong- and weak-shear interfaces (Fig. 2). The relatively strong-shear interface was achieved through using the popular SiO_2 to support the monolayer graphene. The relatively weak-shear interface was accomplished by fabricating graphene drumheads over a graphite substrate (Fig. 2a) as the graphene-graphite interface is believed to be highly lubricated and susceptible to slippage (Hod *et al.*, 2018). The fabrication methods are the same as those described in (Dai *et al.*, 2018). In Fig. 2b, we plot the measured indentation force-deflection relation for the graphite-supported graphene (pink circles), together with the SiO_2-supported graphene extracted from literature (green squares) (Dai *et al.*, 2019). As expected, the "falling through" comes earlier than the SiO_2–supported graphene. This experimental observation confirms that the structural softening is much more significant in the weak-shear indentation. These results highlight the critical role played by the sheet-substrate interface in the indentation tests, particularly at large deformations.

2.3. Elastic instabilities

In addition to modifying the mechanical response, the interfacial slippage can shrink a material circle and cause hoop compressions to the thin sheet. While the compressive stress might be maintained in the supported region due to the confinement of interfacial adhesion, it prefers to be released in the suspended region via the formation of radial wrinkles (Vella, 2019). Compared with wrinkles due to residual compressive stress which gradually disappear with loading (Small and Nix, 1992; Janssens et al., 2020), wrinkles due to sliding are absent initially and only appear after interfacial slippage is initiated to certain extent by loading (we shall show this shortly). The slippage induced wrinkling pattern is visible in the atomic force microscope (AFM) amplitude images of a pressurized graphene sheet in Fig. 3a. So far, there is no evidence for such instabilities occurring in indentation tests due to difficulties in visualizing deformed configurations. However, wrinkling is observable in an alternative system—2D material tents—that could form spontaneously when the sheet is draped over a nanoparticle/pillar-patterned substrate (Dai *et al.*, 2020b; Jiang *et al.*, 2017;

Reserbat-Plantey *et al.*, 2014). Surrounding the tent, radial buckle delamination has been observed in the supported region (Fig. 3b). In general, 2D material tent can be regarded as an inversed, upward indentation. Nevertheless, we should note that different from the tent system whose interface forms via a healing process, the delamination in indentation tests is more likely to be suppressed to avoid the sheet-substrate separation (we will discuss this more in Section 5.1).

In this work, we neglect the pretension and focus on the previously mysterious interfacial slippage, particularly its effect on the mechanical responses of thin sheets upon poking and bulging. Motivated by experimental observations in Section 2, we develop a theory accounting for a finite shear resistance at the sheet-substrate interface as well as elastic instabilities in the sheet in Section 3. Section 4 presents the numerical and analytical results. We will show in Section 5 that our assumptions are not that limited. We will identify a few useful parameters that do not rely on pretension or any specific interfacial traction-separation laws and discuss how they can enable a reliable measure for the elasticity of the thin sheets.

3. Theory

3.1. Problem description

Fig. 4 depicts possible configurations of indented and pressurized thin sheets with the consideration of the interfacial slippage. We use R to denote the radius of the hole. The sheet is suspended in $[0, R]$ while supported by the substrate in $[R, \infty]$ (i.e., infinite size). We assume a constant shear traction at the sheet-substrate interface within the sliding zone $[R, R_o]$. A similar assumption has been used to explain the stress transfer problem in which the substrate is stretched and the strain transferred to the sheet is monitored via Raman spectroscopy (Jiang *et al.*, 2014; Yu *et al.*, 2020). We note that this assumption may be appropriate for common substrates such as polymer and SiO_2. When the substrates are crystalline such as graphite, the constant traction may be considered as the average shear over a domain in which both the dimension and the radial displacement are much larger than $\sqrt{3}a$, where a is the lattice constant (Kumar *et al.*, 2016; Kumar *et al.*, 2015).

We consider three specific cases for the poking and bulging of thin sheets. Case I describes the base state that does not account for instabilities in the thin sheet. This case is thus appropriate only when instability is absent or in its very early stage. As the size of the sliding zone R_o grows with the applied pressure or point force, wrinkles may initiate in $[R_w, R]$, so that the compression in the thin sheet is relieved. We consider this situation in Case II. Note that this case allows the supported part of the sheet to be compressed due to the sheet-substrate interactions, which may be appropriate for most indentation and bulge tests. In Case III, we consider the sheet being confined by a weak adhesion, so that buckle delamination occurs in $[R, R_b]$ in addition to wrinkles in $[R_w, R]$. Case III of poking may better characterize the tent problem (see Fig. 3b) than the indentation problem because tents are formed as the sheets approach the substrates, during which buckle delamination could occur without needing to overcome much energy barrier.

3.1.1. FvK equations

We first discuss the force equilibrium in the suspended, instability-free region, i.e. $[0, R_w]$ ($R_w = R$ in Case I). The load $q(r)$, which is $F\delta(r)/(2\pi r)$ for a point force and p for a pressure, is balanced by the bending and stretching of the sheet (Mansfield, 2005),

$$\nabla^2\left(B\nabla^2 w\right) - (N_{rr}\kappa_{rr} + N_{\theta\theta}\kappa_{\theta\theta}) - q(r) = 0, \tag{3.1}$$

where B is the bending stiffness of the sheet, w is the out-of-plane deflection, N_{rr} (κ_{rr}) and $N_{\theta\theta}$ ($\kappa_{\theta\theta}$) are the radial and hoop stress resultants (curvatures), respectively. For the point force, we use $q(r) = F\delta(r)/2\pi r$ though the force is downward in the diagram in Fig. 1a because the equilibrium equation is invariant under $w \to -w$ and $q \to -q$. We follow the conventional assumptions adopted when analyzing 2D materials indentation and bulging – moderate rotation, linear elasticity, and axisymmetry (Komaragiri *et al.*, 2005; Lee *et al.*, 2008; Mansfield, 2005), such that $\nabla^2 f = d^2 f/dr^2 + r^{-1}df/dr$ and the curvatures approximate

$$\kappa_{rr} \approx \frac{d^2 w}{dr^2} \text{ and } \kappa_{\theta\theta} \approx \frac{dw}{r dr}. \tag{3.2}$$

The in-plane force balance leads to

$$\frac{d}{dr}(rN_{rr}) - N_{\theta\theta} = 0. \tag{3.3}$$

The equilibrium equations with linearized curvatures are often termed the Föppl–von Kármán (FvK) equations. We introduce the Airy stress function ϕ such that the in-plane equilibrium is satisfied automatically by calculating the radial and circumferential stress via

$$N_{rr} = \frac{d\phi}{r dr} \text{ and } N_{\theta\theta} = \frac{d^2\phi}{dr^2}. \tag{3.4}$$

FvK equations can then be rewritten in terms of ϕ and w (Mansfield, 2005),

$$\nabla^2\left(B\nabla^2 w\right) - [\phi, w] - q(r) = 0 \tag{3.5}$$

and

$$\nabla^4 \phi + \frac{1}{2} E_{2D}[w, w] = 0,\tag{3.6}$$

where $[f, g] = \frac{d}{r dr} \left(\frac{df}{dr} \frac{dg}{dr} \right)$. Eq. (3.6) ensures compatibility.

3.1.2. Non-dimensionalization

The stiffness E_{2D} is a constant under the linear elasticity assumption, and the radius R is prescribed by the dimension of the holes pre-patterned on the substrate. We thus use them to normalize variables, including

$$\delta = \frac{d}{R}, \rho = \frac{r}{R}, \rho_o = \frac{R_o}{R}, W = \frac{w}{R}, H = \frac{h}{R}, u = \frac{u}{R}, \rho_w = \frac{R_w}{R}, \rho_b = \frac{R_b}{R}\tag{3.7a}$$

and

$$T = \frac{\tau R}{E_{2D}}, \widetilde{N}_\rho = \frac{N_{rr}}{E_{2D}}, \widetilde{N}_\theta = \frac{N_{\theta\theta}}{E_{2D}}, \mathscr{F} = \frac{F}{E_{2D}R}, P = \frac{pR}{E_{2D}}, \Phi = \frac{\phi}{E_{2D}R^2},\tag{3.7b}$$

where u is the in-plane displacement, and τ represents the constant shear traction. We can then obtain the dimensionless form of the FvK equations

$$\nabla^2 \left(\mathscr{K}^{-1} \nabla^2 W \right) - [\Phi, W] - Q = 0\tag{3.8}$$

and

$$\nabla^4 \Phi + \frac{1}{2} [W, W] = 0,\tag{3.9}$$

where Q is $\mathscr{F}\delta(\rho)/(2\pi\rho)$ for the point force and P for the pressure, and

$$\mathscr{K} = \frac{E_{2D}R^2}{B}\tag{3.10}$$

is often referred to as the FvK number (Blees *et al.*, 2015), which can be thought of as the bendability of the system since sheets with higher FvK numbers are more susceptible to bending than stretching. The compatibility Eq. (3.9) indicates that $\Phi \sim \delta^2$. Thus, the stretching term dominates in (3.8) when $\mathscr{K}^{-1} \ll \delta^2$, or bending effect becomes negligible when $\delta \gg \mathscr{K}^{-1/2}$. This criterion can be readily satisfied in 2D material experiments. In particular, unlike classical plates that resist bending deformations via tension and compression across the neutral plane, monolayer 2D materials resist stretching by the strong in-plane covalent bonds and bending by a different physical origin–weak out-of-plane π bonds (Zhang *et al.*, 2011). This unique behavior causes a much smaller bending stiffness for 2D materials than the prediction by classical plate theory and hence an extremely high bendability in the poking and bulging problems (Han *et al.*, 2020; Wang *et al.*, 2019). For example, the $\mathscr{K}$ of a monolayer graphene with a radius of ~1 μm is ~10^8 (Androulidakis *et al.*, 2018). In what follows, we thus neglect the bending term in (3.8). This simplification is often referred to as the membrane limit of the FvK equations.

3.2. Poking: The base state

Motivated by the extensive use of the indentation tests on 2D materials, we detail the three cases of the poking problem. The formulations can be extended for the bulging problem, which will be discussed briefly in Section 3.5. According to Schwerin's solution (Schwerin, 1929), we expect a $\rho^{-1/3}$ singularity of stresses in the point-loaded sheet as $\rho \to 0$, though the slippage may slightly ameliorate this singularity. It is convenient for numerical computations to introduce

$$\Psi = \rho\Phi', \widetilde{N}_\rho = \frac{\Psi}{\rho^2} \text{ and } \widetilde{N}_\theta = \frac{\Psi'}{\rho} - \frac{\Psi}{\rho^2}\tag{3.11}$$

such that the variable Ψ becomes regular, where ()' denotes differentiation with respect to ρ. With (3.11), the membrane limit of the FvK equations for the poking problem reads

$$\Psi W' = -\frac{\rho\mathscr{F}}{2\pi}\tag{3.12}$$

and

$$\Psi'' - \frac{\Psi'}{\rho} = -\frac{1}{2}W'^2,\tag{3.13}$$

which can be obtained through integrating (3.8) and (3.9) over $[0, \rho]$ once. The integration constants are null because, unlike a plate,

the suspended sheet experiences no transverse or shear forces. For a prescribed point force $\mathscr{F}$, the equations are to be solved with three boundary conditions. The zero in-plane deformation at the center and zero out-of-plane deformation at the edge give

$$\lim_{\rho \to 0} \varkappa = 0 \text{ and } W(1) = 0, \tag{3.14}$$

respectively. The third condition should match the continuity of the displacement across the edge of the hole, which needs a bit of thought.

Within the supported domain, i.e., $\rho \in [1, \rho_o]$, the only equilibrium equation comes from the in-plane force balance,

$$\frac{d}{d\rho}\left(\rho\widetilde{N}_\rho\right) - \widetilde{N}_\theta + T\rho = 0. \tag{3.15}$$

Assuming constant interfacial shear traction as well as linear elasticity for this flat region, we can rewrite (3.15) in terms of $\widetilde{N}_\rho$,

$$\rho\widetilde{N}_\rho'' + 3\widetilde{N}_\rho' + (2+\nu)T = 0. \tag{3.16}$$

We obtain the exact solution to this plane-stress problem, given that both stresses become zero at $\rho \to \rho_o$ (pretension is neglected),

$$\widetilde{N}_\rho = T\left(\frac{1+\nu}{2}\rho_o + \frac{1-\nu}{6}\rho_o^3\rho^{-2} - \frac{2+\nu}{3}\rho\right), \tag{3.17}$$

which, together with (3.15), gives rise to

$$\widetilde{N}_\theta = T\left(\frac{1+\nu}{2}\rho_o - \frac{1-\nu}{6}\rho_o^3\rho^{-2} - \frac{1+2\nu}{3}\rho\right). \tag{3.18}$$

The clamped boundary condition is a special situation when the sliding zone vanishes, i.e., $\rho_o \to 1$. In this situation, $\lim_{\rho_o \to 1}\widetilde{N}_\theta(1^+)$ / $\widetilde{N}_\rho(1^+) = \nu$, implying zero circumferential strain or zero in-plane displacement at the edge of the hole.

The radial stress and in-plane displacement are continuous across the edge of the hole, leading to

$$\Psi(1) = T\left(\frac{1-\nu}{6}\rho_o^3 + \frac{1+\nu}{2}\rho_o - \frac{2+\nu}{3}\right) \tag{3.19}$$

and

$$\Psi'(1) - (1+\nu)\Psi(1) = \frac{T}{6}(\nu^2 - 1)(\rho_o - 1)^2(\rho_o + 2). \tag{3.20}$$

With a prescribed point force and given interfacial shear traction, the four conditions in (3.14), (3.19), and (3.20) can be used to solve the coupled ODEs in (3.12) and (3.13) as well as the unknown sliding extent ρ_o.

3.3. Poking: Strong adhesion

When wrinkling occurs in the suspended region and modifies the stress state, we consider a transition from Case I to Case II (Fig. 4b). Case II may be the most common situation in nanoindentation tests of 2D materials where the center deflection is moderate ($\delta \lesssim 0.3$) and the sheet-substrate normal interaction is strong enough to suppress the wrinkling in the supported region. Due to the wrinkling, the domain where regular FvK equations are applicable shrinks to $[0, \rho_w]$. The solution to the plane stress problem in the supported region still holds as we assume no wrinkling. In the wrinkled zone $[\rho_w, 1]$, we adopt the tension field theory (TFT) to describe the stress state, assuming that the hoop compression in this domain is fully released. The second FvK equation concerning the compatibility is then replaced by a zero hoop stress. This assumption should be valid for 2D materials due to their atomic thinness. The vertical force balance in (3.8) becomes

$$(\Phi' W')' = 0. \tag{3.21}$$

Based on the in-plane force balance with $\widetilde{N}_\theta = 0$, we obtain the solutions to (3.21),

$$\Phi' = C_N \text{ and } W = C_W(1 - \rho), \tag{3.22}$$

where we have used $W(1) = 0$. Eq. (3.22) suggests a zero Gaussian curvature in the wrinkling zone. The problem now is to solve the regular FvK equations along with the four unknown constants (i.e., ρ_w, C_N, C_W, and ρ_o), which requires seven boundary and continuity conditions.

The condition in (3.14) regarding zero in-plane displacements at the center still holds. The continuity conditions at the inner and outer edges of the wrinkled zone should be enforced. We then have

$$\lim_{\rho \to 0} u = 0 \text{ and } [W]_{\rho_w^-}^{\rho_w^+} = [W']_{\rho_w^-}^{\rho_w^+} = \left[\widetilde{N}_\rho\right]_{\rho_w^-}^{\rho_w^+} = \left[\widetilde{N}_\rho\right]_{1^-}^{1^+} = 0, \tag{3.23}$$

where $[x]_-^+ = x^+ - x^-$. As the hoop compression is maintained in the supported region, we expect a jump of hoop stress across the edge of the hole. However, such jump is not allowed at the inner radius of the wrinkled zone, leading to

$$\left[\widetilde{N}_\theta\right]_{\rho_w^-}^{\rho_w^+} = 0. \tag{3.24}$$

This hoop stress continuity in the suspended region has been proved to be equivalent to the minimization of total elastic energy with respect to ρ_w in similar problems utilizing the TFT (Davidovitch et al., 2011; King et al., 2012). The wrinkling zone is much like a plastic zone – it grows with increasing load, and its initiation criterion provides a continuity condition at the growing front. The final condition is related to the in-plane displacement, whose solution has been missing in the wrinkled region. We use the kinematics and Hooke's law in the wrinkled region,

$$\varepsilon_\rho = u' + \frac{1}{2}(W')^2 = \widetilde{N}_\rho - \nu \widetilde{N}_\theta, \tag{3.25}$$

to show that

$$u(\rho_w^+) - u(1^-) = C_N \ln \rho_w + \frac{1}{2} C_W^2 (1 - \rho_w), \tag{3.26}$$

where we used (3.22). The displacements on the right side of (3.26) can be calculated according to the stress states in the unwrinkled regions since $[u]_{\rho_w^-}^{\rho_w^+} = [u]_{1^-}^{1^+} = 0$. Eqs. (3.23), (3.24), and (3.26) complete the seven conditions that are required in Case II.

3.4. Poking: Weak adhesion

In Case III, we consider that instabilities arise and release the hoop compression in both suspended and supported regions (Fig. 4c). Within the suspended region, we use the wrinkled and unwrinkled theories developed in Case II. In the supported domain, the problem is much complicated by the fact that the instability could take various forms of buckle delamination, which will be discussed in Section 5.1. We do not elucidate this complication since Case III is not likely to occur in indentation (as well as bulge) tests (also see discussions in Section 5.1). However, to gain quantitative insights into the delamination effect on the load-deflection behavior, we consider the most straightforward situation – a weak-adhesion interface. Specifically, we assume that any compressive force can cause the sheet to delaminate from its substrate so that the TFT is applicable in the buckle delamination zone $[1, \rho_b]$ as well. The stiffness of the sheet upon poking calculated under this assumption can thus be thought of as a lower limit.

The size of the buckled zone is determined by $\widetilde{N}_\theta(\rho_b) = 0$, which, according to (3.18), requires

$$\frac{\rho_o^2}{\rho_b^2} + \frac{2(1 + 2\nu)}{1 - \nu}\frac{\rho_b}{\rho_o} - \frac{3(1 + \nu)}{1 - \nu} = 0. \tag{3.27}$$

Eq. (3.27) is meaningful only when $\rho_b \geq 1$, i.e.,

$$\rho_o \geq \rho_\nu = \frac{\sqrt{9 + 6\nu - 15\nu^2} - 1 - \nu}{2(1 - \nu)}. \tag{3.28}$$

This criterion also characterizes the critical size of the sliding zone beyond which hoop stress becomes compressive, and instability is expected to initiate. Correspondingly, $\rho_o \gtrsim 1.35$ for graphene with $\nu = 0.165$. In the unbuckled region $[\rho_b, \rho_o]$, (3.17) and (3.18) can be used while in the buckled region $[1, \rho_b]$, we rewrite the in-plane Eq. (3.15) with released hoop stress:

$$\frac{d}{d\rho}\left(\rho \widetilde{N}_\rho\right) + T\rho = 0. \tag{3.29}$$

As a consequence, the problem is to solve the regular FvK equations and (3.29) as well as five unknowns (i.e., $\rho_w, C_N, C_W, \rho_b,$ and ρ_o), which requires nine boundary and continuity conditions.

According to the zero in-plane displacement at the center and the continuity conditions, we have
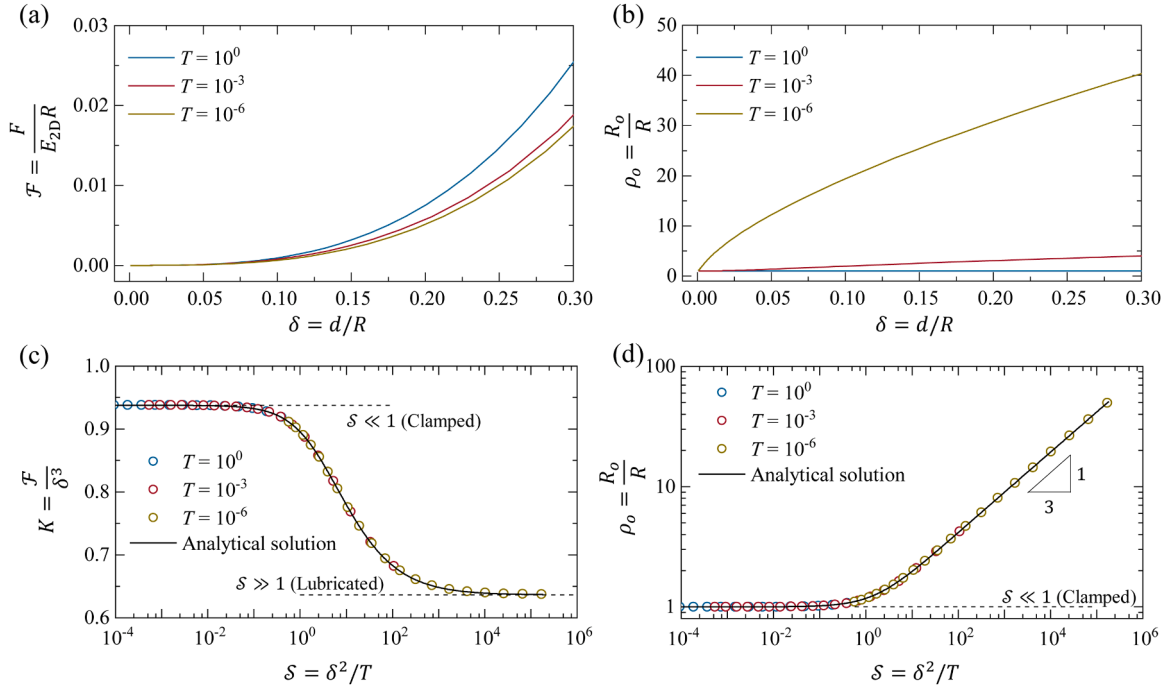
$$\lim_{\rho \to 0} u = 0, \tag{3.30a}$$

and

$$[W]_{\rho_w^-}^{\rho_w^+} = [W']_{\rho_w^-}^{\rho_w^+} = \left[\widetilde{N}_\rho\right]_{\rho_w^-}^{\rho_w^+} = \left[\widetilde{N}_\theta\right]_{\rho_w^-}^{\rho_w^+} = \left[\widetilde{N}_\rho\right]_{1^-}^{1^+} = \left[\widetilde{N}_\rho\right]_{\rho_b^-}^{\rho_b^+} = 0. \tag{3.30b}$$

We note that $[\widetilde{N}_\theta]_{1^-}^{1^+} = 0$ has been satisfied automatically, and $[\widetilde{N}_\theta]_{\rho_b^-}^{\rho_b^+} = 0$ amounts to (3.27). Again, the last condition comes from the

Fig. 5. (a) Indentation force-deflection curves for thin sheets with various interfacial shear tractions provided by their substrates. Note that the result of $T = 1$ shows no discernable difference to that based on clamped boundary conditions. (b) The sliding extent as a function of the center deflection under various interfacial shear tractions. The dependency of the effective stiffness (c) and the sliding extent (d) on the sliding number. Markers are obtained by numerical calculations, while solid curves are from analytical solutions detailed in Appendix B.

continuity of the in-plane displacement across the wrinkled and buckled regions,

$$\varkappa\left(\rho_w^+\right) - \varkappa\left(\rho_b^+\right) = C_N \ln\rho_w + \frac{1}{2}C_W^2(1 - \rho_w) + \int_{\rho_b^+} \widetilde{N}_\rho d\rho, \tag{3.31}$$

where the displacements on the right side can be calculated according to the stress states in the unwrinkled/unbuckled regions since $[\varkappa]_{\rho_w}^{\rho_w^+} = [\varkappa]_{\rho_b}^{\rho_b^+} = 0$. Eqs. (3.27), (3.30), and (3.31) complete the conditions necessary to solve the boundary value problem in Case III.

3.5. From poking to bulging

The analysis of the bulging problem follows the same techniques outlined for the poking problem in the previous sections. In particular, the ODEs are identical in the supported region. The main changes come from differences between point-loaded and pressurized sheets in the vertical force balance. For the bulging problem, the membrane limit of FvK equations, according to (3.8), could be written as

$$\Phi W' = -\frac{1}{2}P\rho^2 \tag{3.32}$$

and

$$\rho\frac{d}{d\rho}\left[\frac{1}{\rho}\frac{d}{d\rho}(\rho\Phi)\right] = -\frac{1}{2}W'^2, \tag{3.33}$$

where we used Φ to substitute Φ'. Eqs. (3.32) and (3.33) are applicable in $[0, \rho_w]$ (though $\rho_w = 1$ in Case I). In the wrinkled region $[\rho_w, 1]$, the hoop stress vanishes, allowing for analytical solutions to the vertical and horizontal equilibrium equations,

$$\Phi = C_N \quad \text{and} \quad W = \frac{P}{6C_N}\left(1 - \rho^3\right), \tag{3.34}$$

$W(1) = 0$ and the continuity of W' at $\rho = \rho_w$ have been enforced in (3.34). Unlike the poking problem, the wrinkled sheet in the bulging problem shows a nonlinear deflection along the radial direction.

Table 1

The asymptotic responses of thin sheets upon poking and bulging. We list the coefficients if they are Poisson's ratio independent, or their dependence is explicit. Otherwise, the coefficients are not provided and just labeled by "~". $\alpha_{\mathscr{F}}(\nu)$ and $\alpha_P(\nu)$ can be found in (1.1) and (1.2), respectively, which were provided by (Komaragiri et al., 2005). ρ_ν is defined by (3.28).

	Poking Case I			Case II				Case III		
Regime	$\mathscr{F}/\delta^3$	ρ_o	Regime	$\mathscr{F}/\delta^3$	ρ_w	ρ_o	$\mathscr{F}/\delta^3$	ρ_w	ρ_o
$\mathscr{S}\lesssim10^{-1}$	$\alpha_{\mathscr{F}}(\nu)$	1	$\mathscr{S}=S_c(\nu)$	0.86	1	ρ_ν	0.86	1	ρ_ν
$\mathscr{S}\gtrsim10^4$	$\dfrac{2}{\pi}$	$\left[\dfrac{6\mathscr{S}}{\pi^2(1-\nu)}\right]^{1/3}$	$\mathscr{S}\gtrsim10^4$	$\dfrac{1.94}{\pi}$	0.49	$\sim\mathscr{S}^{1/3}$	$\sim(\ln\mathscr{S})^{-1/2}$	$\sim(\ln\mathscr{S})^{-1}$	$\sim\mathscr{S}^{1/2}$
	Bulging Case I			Case II			Case III		
	P/δ^3	ρ_o		P/δ^3	ρ_w	ρ_o	P/δ^3	ρ_w	ρ_o
$\mathscr{S}\lesssim10^{-2}$	$\alpha_P(\nu)$	1	$\mathscr{S}=S_c(\nu)$	2.69	1	ρ_ν	2.69	1	ρ_ν
$\mathscr{S}\gtrsim10^3$	1.63	$\sim\mathscr{S}^{1/3}$	$\mathscr{S}\gtrsim10^4$	1.60	0.86	$\sim\mathscr{S}^{1/3}$	NA	NA	$\sim\mathscr{S}^{1/2}$

4. Results

4.1. Poking: Emergence of a sliding number

We begin by discussing Case I of the poking problem. Fig. 5a plots numerically solved indentation force-deflection curves for thin sheets with various shear tractions provided by their substrates. As expected, thin sheets with weaker shear traction behave less resistive to the point force. To indicate the poking resistance, we define an effective stiffness of the system,

$$K = \frac{\mathscr{F}}{\delta^3}. \tag{4.1}$$

K should be a strong function of the sliding extent, as plotted in Fig. 5b, which depends on not only the shear traction (that resists the slippage) but also the deflection (that drives the slippage). To better characterize the sliding extent, we propose a new parameter – the sliding number that compares the driving force with the resistive force,

$$\mathscr{S} = \frac{\delta^2}{T}, \tag{4.2}$$

where the square is used because the sheet tension scales as δ^2 (Chen, 2020; Vella and Davidovitch, 2017). Apparently, thin sheets with larger sliding numbers undergo further interfacial slippage.

The use of the sliding number can collapse the numerical results on the effective stiffness of thin sheets with various deflections and interfacial tractions into a master curve (Fig. 5c). We find two limits: when the interfacial slippage is negligible or when the interfacial shear traction is negligible. Fig. 5c clearly suggests that the sheet is close to being clamped when $\mathscr{S}\lesssim0.1$ while the sheet-substrate interface is close to being ultra-lubricated or frictionless when $\mathscr{S}\gtrsim10^4$.

We also found analytical solutions for the master $K-\mathscr{S}$ curve in Fig. 5c (see the derivation in Appendix B). The effective stiffness can be expressed as

$$K = \frac{\pi}{2}\frac{\theta_1-(1-\psi_1)\tan\theta_1}{\theta_1^3}, \tag{4.3}$$

where $\theta_1 = \tan^{-1}[\psi_1^{1/2}/(1-\psi_1)^{1/2}] \leq \pi/2$. The intermediate parameter ψ_1 is controlled by $\mathscr{S}$ and can be solved simply based on two algebraic equations:

$$3\psi_1\mathscr{S}/\theta_1^2 = 6(1+\nu)\rho_o + 2(1-\nu)\rho_o^3 - 4(2+\nu) \tag{4.4}$$
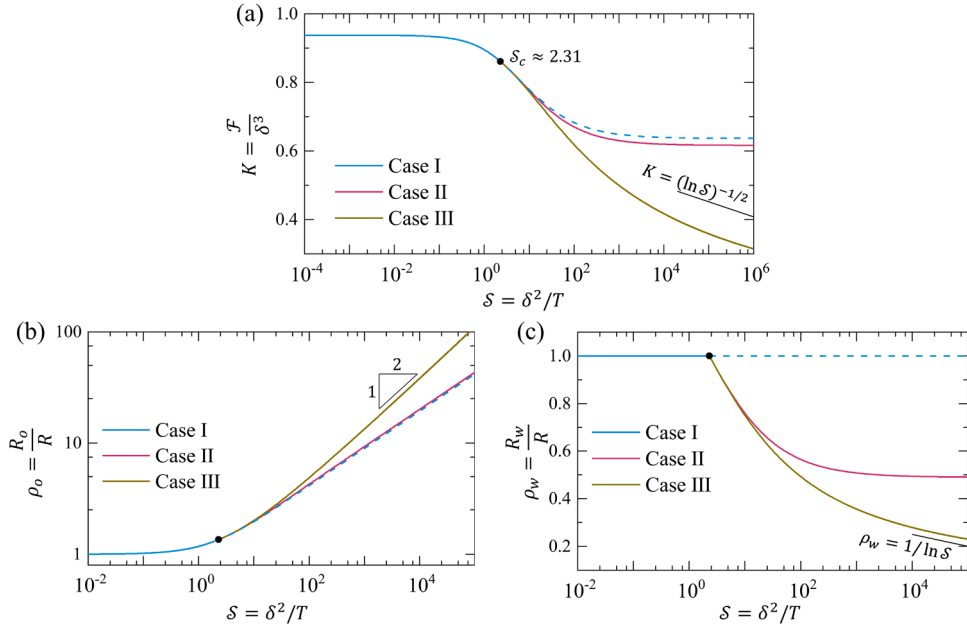
and

$$2(1+\nu)\theta_1^2(\rho_o-1)/\mathscr{S} - \theta_1/\tan\theta_1 - \psi_1 + 1 = 0. \tag{4.5}$$

The two equations also indicate a master $\rho_o - \mathscr{S}$ curve, which is plotted in Fig. 5d.

The analytical solution is very beneficial to understand the asymptotic behaviors of the system, emerging under small or large sliding numbers, which are called strong-shear and weak-shear limits, respectively:

$$K \approx \begin{cases} \alpha_{\mathscr{F}}(\nu), & \mathscr{S}\lesssim0.1 \\ 2/\pi, & \mathscr{S}\gtrsim10^4 \end{cases} \tag{4.6}$$

Fig. 6. The dependency of the effective stiffness (a), the sliding extent (b), and the wrinkling extent (c) on the sliding number in all three cases. Dots label the critical points from Case I to Case II (strong adhesion) or to Case III (weak adhesion). Dashed curves represent unrealistic Case I solutions after instability sets in.

and

$$\rho_o(\mathscr{S}) approx \begin{cases} 1, & \mathscr{S} \lesssim 0.1 \\ \left[\dfrac{6\mathscr{S}}{\pi^2(1-\nu)}\right]^{1/3}, & \mathscr{S} \gtrsim 10 \end{cases}.$$ (4.7)

The limits, together with these in other cases discussed shortly, are summarized in Table 1. We find good agreement between $\alpha_{\mathscr{F}}(\nu)$ in (1.1), and numerical calculations (Fig. 5c). It is also found that the large-$\mathscr{S}$ stiffness is surprisingly simple and is independent of Poisson's ratio. However, the weak-shear limit of Case I is not realistic for ultrathin sheets as elastic instabilities should initiate much earlier than this limit.

4.2. Poking: Role of instabilities

We then move on to discuss the mechanical responses when elastic instabilities set in. It is well known that the tangential interaction between 2D materials and their substrate is much weaker than their normal interaction (Dai et al., 2020a). This contrast drives the scenario of Case II: the sheet wrinkles in the suspended region and remains flat in the supported region. We perform numerical calculations following the formulation in Section 3.3 and identify the sliding number still to be the sole controlling parameter of Case II. In Fig. 6, we display the $\mathscr{S}$-dependency of the effective stiffness (Fig. 6a) as well as the sliding extent (Fig. 6b) and the wrinkling extent (Fig. 6c) (More rigorously, $1 - \rho_w$ is the wrinkling extent).

The critical point separating Case I and Case II is located at $\mathscr{S} = \mathscr{S}_c$, since which the hoop stress at the edge becomes compressive. The value of $\mathscr{S}_c$ is very sensitive to Poisson's ratio because the onset of instability needs the shrinkage of a material circle due to the radial sliding to be larger than that due to the Poisson's effect. The results in Fig. 6 are based on graphene of $\nu = 0.165$ (correspondingly, $\mathscr{S}_c \approx 2.306$). After this point, radial wrinkles grow from the edge of the hole towards the center (Fig. 6c), along with a further softened poking resistance (Fig. 6a). When the sliding number is sufficiently large (i.e., $\mathscr{S} \gtrsim 10^4$), the weak-shear limit emerges. Consequently, the effective stiffness stabilizes, and the radial wrinkles extend to their maximum length (not reaching the hole center, see detailed values in Table 1). Compared with Case I, Case II shows a smaller stiffness at large sliding numbers (Fig. 6a), due to the release of hoop stresses. However, the difference is minor (~3%), implying that the wrinkling only modifies radial stresses slightly.

These results can qualitatively explain the softening behavior observed in Fig. 1. In particular, experimental results lie in between the strong-shear limit of Case I and the weak-shear limit of Case II when deflections are relatively large. A quantitative interpretation of these results is challenging and also subjected to considerable fitting errors because of the complex interplay between pretension and interfacial slippage. Alternatively, we will present a different method in the discussion section allowing for simpler metrology of the elasticity of the thin sheet.

We succeed in deriving exact analytical solutions for master relations in Case II (see details in Appendix C). The effective stiffness is
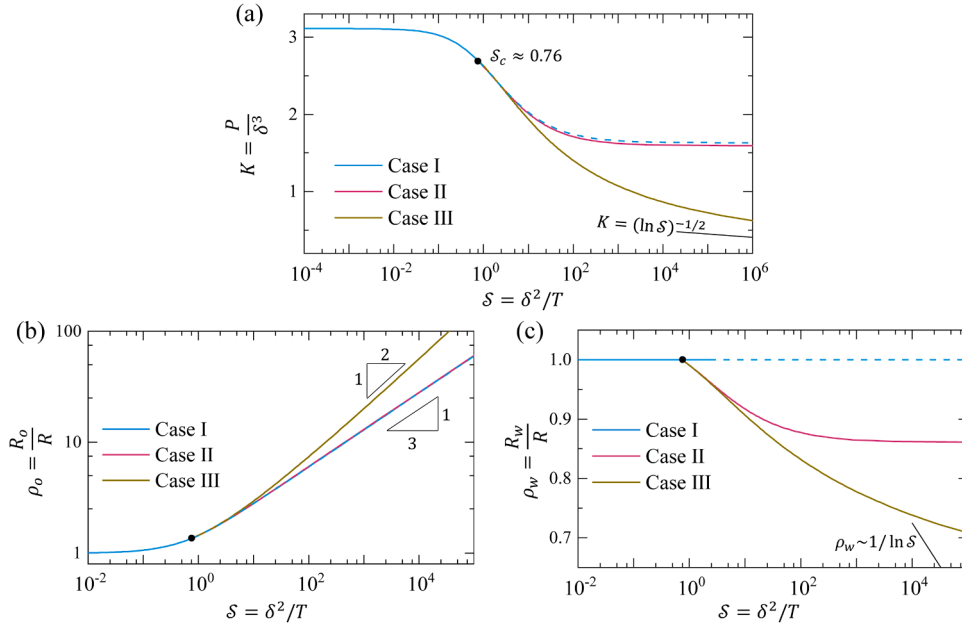
Fig. 7. The dependency of the effective stiffness (a), the sliding extent (b), and the wrinkling extent (c) on the sliding number for the three cases in the bulging problem. Again, dots label the critical points from Case I to Case II or to Case III.

found to depend on the size of the wrinkled zone,

$$K = 2\pi\psi_w\rho_w\tan\theta_w[(1 - \rho_w)\tan\theta_w + 2\rho_w\theta_w]^{-3}, \qquad (4.8)$$

where $\theta_w = \tan^{-1}[\psi_w^{1/2}/(1 - \psi_w)^{1/2}]$ and ψ_w is an intermediate constant. The vanishing hoop stress at the end of the wrinkling zone gives a transcendental equation for ψ_w,

$$(2 - \psi_w)\tan\theta_w - 2\theta_w = 0, \qquad (4.9)$$

whose solution is $\psi_w \approx 0.6965$. ρ_w, characterizing the wrinkling extent, can be solved based on algebraic equations (C.10) and (C.11) in the Appendix. These equations also prove the master $\rho_o - \mathscr{S}$ relation, particularly that $\rho_o \sim \mathscr{S}^{1/3}$ at large sliding numbers. Besides, the asymptotic analysis suggests a number of quantities that are independent of Poisson's ratio (Table 1), including the upper limit of the wrinkling extent, i.e., the smallest possible $\rho_w(\mathscr{S} \to \infty)$, and the effective stiffness at the critical moment of wrinkling, i.e., $K(\mathscr{S} = \mathscr{S}_c)$, and the saturation of wrinkling, i.e., $K(\mathscr{S} \to \infty)$.

We have shown that wrinkling plays a small role in the mechanical response of the sheet in Case II. However, elastic instabilities would dramatically modify the sheet response in Case III (Fig. 6), where we assume that the adhesion is weak, and the instability occurs in both suspended and supported regions as long as the material is in compression. Under this assumption, we still find $\mathscr{S}$ to be the only controlling parameter. Due to buckle delamination, the sliding and wrinkling zones propagate with respect to $\mathscr{S}$ in a much faster manner (Fig. 6b and 6c). Specifically, for Case III of large sliding numbers, ρ_o scales as $\mathscr{S}^{1/2}$ ($\mathscr{S}^{1/3}$ in Case I and II); Instead of being a constant, ρ_w scales as $1/\ln\mathscr{S}$. Consequently, $\mathscr{T} \sim \delta^3/\sqrt{\ln\mathscr{S}}$ – the effective stiffness fails to stabilize (see Fig. 6a).

These scaling relations are based on the exact solution to Case III (Appendix D). Interestingly, the simple relation in (4.8) is also applicable to Case III while ρ_w and ρ_o are determined by a different set of equations – (D.4) and (D.6). In Case I or II, there exists a weak-shear limit so that one may use a large $\mathscr{S}$ to calculate parameters (such as the effective stiffness and the wrinkling extent) for systems with vanishing friction. However, our theory for Case III cannot provide predictions for infinitely large $\mathscr{S}$. This issue could be tackled by considering the finite lateral size of a thin sheet since the sliding zone engulfs the sheet if the interfacial shear traction is zero (Davidovitch and Guinea, 2020). However, we are not going to do so as there are many difficulties to fully understand the physics in the supported region, as discussed in Section 5.1 and 5.2.

4.3. Bulge tests

For thin sheets in bulge tests, the sliding number still enables the plot of the master curves. We show the numerically calculated effective stiffness (defined by $K = P/\delta^3$) and the sliding and wrinkling extent in Fig. 7. Though we failed to obtain analytical solutions, most of the asymptotic responses we derived for the poking problem are found applicable to the bulging problem. For instance, the two limits appear in Case I and Case II: the sheet-substrate interface is nearly clamped when $\mathscr{S} \lesssim 10^{-2}$ and frictionless when $\mathscr{S} \gtrsim 10^3$. The

critical sliding number $\mathscr{S}_c$ for the I-II transition of a graphene sheet is ~ 0.76 (Fig. 7a). We checked numerically that $K(\mathscr{S}_c)$ is ~ 2.79 and ν-independent. At large sliding numbers, we can identify the $\rho_o \sim \mathscr{S}^{1/3}$ relation (Fig. 7b) as well as the ν-independent $K(\mathscr{S} \to \infty)$ in Case I and II (Table 1).

Compared with point force, thin sheets under pressure show even smaller differences between Case I and Case II: the $\rho_o - \mathscr{S}$ relation nearly overlaps (Fig. 7b), and the weak-shear stiffness only differs by 1.9% (Fig. 7a). The reason for this limited effect of wrinkling is the limited length of the wrinkles $(1 - \rho_w)$, which is up to 0.51 in a point-loaded sheet and only 0.14 in a pressurized sheet. In bulge experiments, the size of the wrinkled zone ranges from ~ 0.06 (Luo *et al.*, 2020) to ~ 0.12 in Fig. 3a (Wang *et al.*, 2017). The different behaviors in ρ_w between poking and bulging is also visible in the asymptotic response of thin sheets with weak adhesive interactions (Case III). We have derived $\rho_w \sim 1/\ln\mathscr{S}$ and $K \sim 1/\sqrt{\ln\mathscr{S}}$ for Case III of the poking problem, leveraging that the wrinkles are reasonably long in this case. These relations are therefore invalid for the bulging problem (Fig. 7a and 7c) although $\rho_o \sim \mathscr{S}^{1/2}$ seems to agree quite well with the numerical results (Fig. 7a).

5. Discussions

Our relatively simple theoretical framework has allowed several important understandings of the mechanical behaviors of atomically thin sheets under poking and bulging. However, our analysis neglects some critical aspects of interface mechanics, including the finite interfacial adhesion, substrate surface roughness, and the mixed-mode delamination. In this section, we discuss the challenges associated with those subtleties and, more importantly, propose an alternative metrology for the elasticity of 2D materials that would be immune to these subtleties.

5.1. Interfacial normal interactions

As mentioned earlier, the analysis of Case III has been unrealistic. To solve Case III, we adopted TFT to release the compression of the buckled sheet in the supported region (essentially assuming no adhesion in the supported region). This treatment has been useful for suspended or water-floating sheets (Davidovitch and Vella, 2018; Vella and Davidovitch, 2018). However, the support of a rigid substrate could help maintain certain compression (Davidovitch *et al.*, 2019). The problem is more complicated when the radial buckle delamination occurs as it is often non-axisymmetric; An additional length scale is needed to characterize the spacing of these buckles, as seen in (Dai *et al.*, 2020b) and discussed in a recent work (Davidovitch and Guinea, 2020).

A recent work studied the wrinkling (instead of delamination) in the supported region by considering the normal sheet-substrate interaction as a linear Winkler foundation (Davidovitch and Guinea, 2020). This treatment would further complicate the hoop stress jump across the edge of the hole. Our analysis for the weak-limit of Case II is identical to the Davidovitch-Guinea analysis with a sufficiently large foundation stiffness. More generally, however, the physics in the supported region is a combination of mechanical properties of the sheet, pretension, and interfacial normal/shear tractions (Davidovitch and Guinea, 2020). When the interfacial shear traction is negligible (for instance, graphene on graphite), Case II is in its weak-shear limit. The corresponding analysis is valid only if the center deflection or the hoop compression at the edge of the hole (that drives the wrinkling in the supported region) is sufficiently small, compared with the bending stiffness of the sheet and the stiffness of the sheet-substrate normal interaction (that resists the wrinkling) (Davidovitch and Guinea, 2020). When the shear traction is nontrivial (for instance, graphene on SiO$_2$), the normal-tangential coupling needs to be considered. In bulge experiments in Fig. 3a, this supported region is found to be relatively "flat"; At least, AFM-based characterizations did not show wrinkles in this region. In indentation experiments, yet again, no observations are available.

5.2. 2D or not 2D

We have assumed that the unbuckled sheet in the supported region is flat and adopted the 2D plane-stress analysis with a body force. This assumption may approximate well when the substrate is crystalline, and the interface is atomically smooth. However, 2D materials in indentation and bulge tests are mostly supported by SiO$_2$, whose surface roughness needs to be considered. This effect on the overall poking or bulging stiffness of the sheet may be negligible since the sliding number in these systems is relatively small ($\mathscr{S} \lesssim 10$, according to $T \sim 0.01$ in the literature) (Kitt *et al.*, 2013; Wang *et al.*, 2017). However, the detailed size of the sliding zone may be significantly influenced by the substrate roughness. This also brings a question of how surface roughness tunes the tangential behavior of sheet-substrate interfaces, which remains an outstanding question (Dai *et al.*, 2020a).

Besides, we have used the simplest tangential traction-separation law – constant traction. Many of our conclusions, including those based on the strong- or weak-shear limit, should be modified by using a different traction-separation law. For instance, indentation and bulge tests are inherently mixed-mode with nonzero normal and shear tractions at the interface (Cao *et al.*, 2015, 2016; Davidovitch and Guinea, 2020). From the point of view of intermolecular interactions, the normal interfacial separation would weaken the tangential traction, possibly leading to an increased sliding number. It is not clear how the sliding modifies the normal traction or vice versa, especially given the complexity due to substrate roughness.

5.3. Wrinkling-assisted metrology

In the introduction, we discussed the difficulties in interpreting the bulge and indentation experiments due to the coupling between
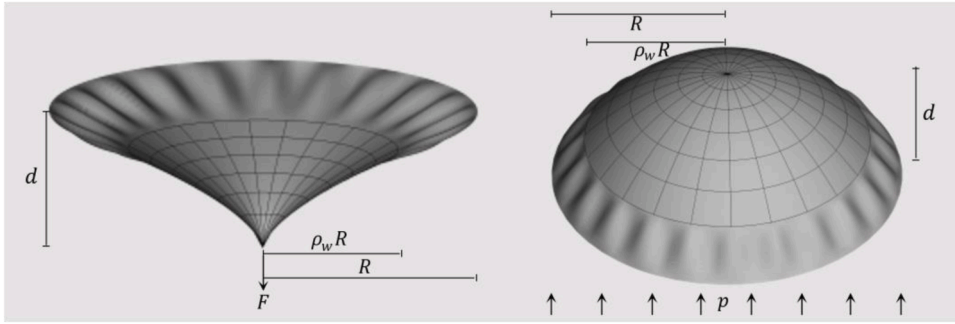
Fig. 8. Schematics of exploiting the wrinkling instabilities in the suspended region in indentation and bulge tests of thin sheets.

pretension and out-of-plane deformation. This work further introduces the complexity associated with the interfacial slippage, which should be particularly significant for ultrathin sheets whose edges are often not perfectly glued. More troubles would arise and make analytical efforts like (1.1) and (1.2) impossible when interface subtleties (such as surface roughness and complicated traction-separation laws) are considered.

Our studies of the poking problem inspire a useful, alternative way to exploit both indentation and bulge tests (Fig. 8). The idea comes from the effective stiffness as a function of the wrinkling extent in Case II, i.e., (4.8). We rewrite the load-deflection relation:

$$
d^3 \approx \begin{cases} \dfrac{(\rho_w + 3.29)^3 F R^2}{68.2 \rho_w E_{2D}} & \text{(Indentation tests)} \\[2ex] \dfrac{pR^4}{(7.95\rho_w - 5.27)E_{2D}} & \text{(Bulge tests)} \end{cases}, \tag{5.1}
$$

where the first equation is based on (4.8), and the second is the fitting of the numerical solution to the bulging problem (Fig. 8). Though ρ_w is related to the sliding number in this work, it, together with the applied load and deflection, are experimentally accessible, leading to a direct measure of the sheet stiffness. Note again that the coefficients in (5.1) are independent of Poisson's ratio of the sheet, pretension, or any specific interfacial laws (the interaction with the substrate could even be absent). The underlying reason is that for a given ρ_w, the condition of zero hoop stress at the tip of the wrinkle allows the solution of the coupled ODEs in the suspended region without matching the continuity conditions at the edge of the hole.

The invariance of (5.1) renders elasticity metrology for thin sheets immune to errors caused by the unknown pretension and Poisson's ratio, which have been troublesome in traditional indentation tests. In addition, by leveraging the mechanical response at the onset of wrinkling, the measure could be achieved without knowing the detailed wrinkling extent, i.e., $\rho_w = 1$. As long as the axisymmetry holds, the adventitious pretension during the material transfer makes no difference, and the substrate could be designed in various forms (not limited to the configurations in Fig. 4). A similar conclusion could be drawn at the late stage of the wrinkling, the signature of which is simply the ripening of the wrinkled zone. ρ_w at this stage in the indentation and bulge tests is constant, as provided in Table 1. However, it would be modified by nonzero pretensions. Alternatively, a theoretical investigation on this modification may offer an opportunity for the measure of the pretension in the sheet. The late-stage usually comes with relatively large deflections. Therefore, one should be cautious about possible material and geometrical nonlinearities (Chandler and Vella, 2020).

6. Concluding remarks

We considered the mechanical response of thin sheets with sliding boundaries upon poking and bulging. When pretension is absent, a sliding number, comparing the membrane tension with the interfacial traction, turned out to be the sole controlling parameter in both problems. We discussed three cases, although Case I and Case II are more likely to occur in indentation and bulge tests. In both cases, we identified the strong- and weak-shear limits: the sheet-substrate interface is nearly clamped at small sliding numbers and ultra-lubricated at large sliding numbers. However, the difference in the effective stiffness between Case I and II is within 3% for all indenting/bulging deflections and theoretically allowable Poisson's ratios. In reality, as the applied load gradually increases, the sheet response is first captured by Case I and transits smoothly to Case II when the hoop stress becomes negative at the edge of the hole. The transition from Case II to III remains to be carefully investigated, especially in tent problems.

Unfortunately, the consideration of edge slippage, together with other factors such as pretension and specific interfacial traction-separation laws, would prevent explicit load-deflection relation like (1.1) and (1.2). It would be a grand challenge to measure the in-plane stiffness of an ultrathin sheet merely using load-deflection curves. A generic yet simple-to-implement poking/bulging methodology has been offered, which leverages the extent of instabilities. We highlighted the robustness of this methodology by its independency of pretension, Poisson's ratio, and any effects associated with the substrate, or even no substrate.
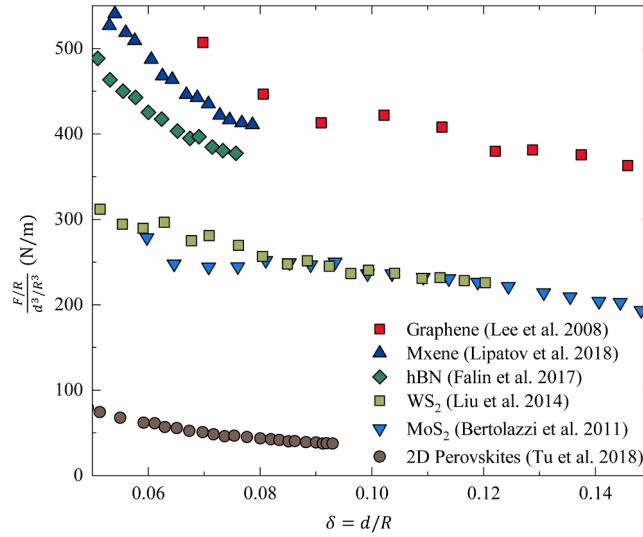
Fig. A1. Rescaled indentation force-deflection relations measured on various 2D materials (Bertolazzi *et al.*, 2011; Falin *et al.*, 2017; Lee *et al.*, 2008; Lipatov *et al.*, 2018; Liu *et al.*, 2014; Tu *et al.*, 2018).

CRediT authorship contribution statement

Zhaohe Dai: Conceptualization, Methodology, Investigation, Formal analysis, Visualization, Writing - original draft. **Nanshu Lu:** Project administration, Supervision, Validation, Writing - review & editing.

Declaration of Competing Interest

The authors declare that they have no known competing financial interests or personal relationships that could have appeared to influence the work reported in this paper.

Acknowledgements

Appendix A. Indentation of various 2D materials

Fig. A1

Appendix B. Analytical solution to Case I

The analytical solution to the nonlinear, coupled FvK Eqs. (3.12) and (3.13) is the key to solve the poking problem (Chopin *et al.*, 2008). The combination of (3.12) and (3.13) leads to

$$\rho \frac{\mathrm{d}}{\mathrm{d}\rho}\left(\frac{1}{\rho}\frac{\mathrm{d}\Psi}{\mathrm{d}\rho}\right) + \frac{1}{2}\left(\frac{\rho\mathscr{F}}{2\pi\Psi}\right)^2 = 0. \tag{B.1}$$

Let $\eta = \rho^2$ so that (B.1) becomes

$$\frac{\mathrm{d}^2\Psi}{\mathrm{d}\eta^2} + \frac{\mathscr{F}^2}{32\pi^2\Psi^2} = 0. \tag{B.2}$$

We integrate (B.2) once to obtain

$$\frac{\mathrm{d}\psi}{\mathrm{d}\eta} = \frac{A^{3/2}\mathscr{F}}{4\pi}\left(\frac{1-\psi}{\psi}\right)^{1/2}, \tag{B.3}$$

where A is the integration constant and $\psi = A\Psi$. Back to (3.12), we find

$$\delta = \int_0^1 \frac{\rho \mathscr{F}}{2\pi \Psi} \, d\rho = \frac{A\mathscr{F}}{4\pi} \int_0^{\psi_1} \frac{d\psi}{\psi \psi'}, \tag{B.4}$$

which can be solved by combining (B.3),

$$\delta = \frac{2}{A^{1/2}} \tan^{-1} \sqrt{\psi_1/(1-\psi_1)}, \tag{B.5}$$

where $\psi' = d\psi/d\eta$ and $\psi_1 = \psi(1)$. There are two ways to determine ψ_1. One is by integrating (B.3) to obtain

$$\frac{A^{3/2}\mathscr{F}}{4\pi} \eta = -\sqrt{\psi(1-\psi)} + \tan^{-1}\sqrt{\psi/(1-\psi)}, \tag{B.6}$$

where we have used $\lim_{\rho \to 0} \mu(\rho) = 0$ that is identical to $\lim_{\eta \to 0} \psi(\eta) = 0$. At the edge of the hole,

$$\frac{A^{3/2}}{4\pi}\mathscr{F} = -\sqrt{\psi_1(1-\psi_1)} + \tan^{-1}\sqrt{\psi_1/(1-\psi_1)}. \tag{B.7}$$

Another way is to leverage the continuity of the radial stress across the edge, i.e., (3.19),

$$\psi_1 = AT\left(\frac{1+\nu}{2}\rho_o + \frac{1-\nu}{6}\rho_o^3 - \frac{2+\nu}{3}\right). \tag{B.8}$$

In addition, the continuity of the radial displacement across the edge can give rise to

$$\frac{d\psi}{d\eta}\Big|_{\eta=1} = AT\frac{1+\nu}{2}(\rho_o - 1), \tag{B.9}$$

which, according to (B.3), can further lead to

$$\frac{A^{1/2}\mathscr{F}}{2\pi(1+\nu)}\left(\frac{1-\psi_1}{\psi_1}\right)^{1/2} = T(\rho_o - 1). \tag{B.10}$$

Given a set of poking force $\mathscr{F}$ and interfacial shear traction T, the unknowns, including δ, ψ_1, A, and ρ_o, can be solved based on (B.5), (B.7), (B.8), and (B.10). We can use (B.5) and (B.7) to show the effective stiffness,

$$K = \frac{\mathscr{F}}{\delta^3} = \frac{\pi}{2}\frac{\tan^{-1}\sqrt{\psi_1/(1-\psi_1)} - \sqrt{\psi_1(1-\psi_1)}}{\left[\tan^{-1}\sqrt{\psi_1/(1-\psi_1)}\right]^3}. \tag{B.11}$$

ψ_1 is dependent on a single parameter—$\mathscr{S}$—since (B.5)$^2 \times$ (B.8) equals to

$$3\psi_1\mathscr{S}\left[\tan^{-1}\sqrt{\psi_1/(1-\psi_1)}\right]^{-2} = 6(1+\nu)\rho_o + 2(1-\nu)\rho_o^3 - 4(2+\nu), \tag{B.12}$$

and (B.7)/(B.10)/(B.5)^2 gives

$$2(1+\nu)(\rho_o - 1)\mathscr{S}^{-1}\left[\tan^{-1}\sqrt{\psi_1/(1-\psi_1)}\right]^2 - \sqrt{(1-\psi_1)/\psi_1}\tan^{-1}\sqrt{\psi_1/(1-\psi_1)} = \psi_1 - 1. \tag{B.13}$$

Appendix C. Analytical solution to Case II

In this case, (B.1–B.3) and (B.6) can still be used in the unwrinkled region $[1,\rho_w]$. At the inner edge of the wrinkling zone, we define $\psi_w = \psi(\rho_w)$. Immediately, (B.6) dictates

$$\frac{A^{3/2}\mathscr{F}}{4\pi}\rho_w^2 = -\sqrt{\psi_w(1-\psi_w)} + \tan^{-1}\sqrt{\psi_w/(1-\psi_w)}, \tag{C.1}$$

and the zero hoop stress requires

$$\frac{A^{3/2}\mathscr{F}}{2\pi}\rho_w^2 = \sqrt{\psi_w^3/(1-\psi_w)}, \tag{C.2}$$

which provides an equation for ψ_w,

$$\psi_w\sqrt{\psi_w/(1-\psi_w)} + 2\sqrt{\psi_w(1-\psi_w)} = 2\tan^{-1}\sqrt{\psi_w/(1-\psi_w)}. \tag{C.3}$$

The continuity of the slope and the radial stress across the wrinkling tip can solve

$$C_w = \frac{A\rho_w \mathscr{F}}{2\pi\psi_w} = \frac{1}{A^{1/2}\rho_w}\sqrt{\frac{\psi_w}{1-\psi_w}} \tag{C.4}$$

and

$$C_N = \frac{\psi_w}{A\rho_w}, \tag{C.5}$$

respectively. The center deflection can be calculated by summing up the wrinkled and unwrinkled parts,

$$\delta = W(\rho_w) + \int_0^{\rho_w} \frac{\rho\mathscr{F}}{2\pi\Psi}\,d\rho = \frac{1}{A^{1/2}}\left(\frac{1-\rho_w}{\rho_w}\sqrt{\frac{\psi_w}{1-\psi_w}} + 2\tan^{-1}\sqrt{\frac{\psi_w}{1-\psi_w}}\right). \tag{C.6}$$

Moving the focus outward, we require the continuity of the radial stress at the edge of the hole,

$$\frac{\psi_w}{AT\rho_w} = -\frac{2+\nu}{3} + \frac{1-\nu}{6}\rho_o^3 + \frac{1+\nu}{2}\rho_o. \tag{C.7}$$

Finally, the displacement condition (3.26) is rewritten as

$$6\psi_w(\nu + \ln\rho_w) + \frac{3\psi_w(1-\rho_w)}{\rho_w(1-\psi_w)} - AT(1-\nu^2)\rho_w(\rho_o+2)(\rho_o-1)^2 = 0. \tag{C.8}$$

We compute the effective stiffness by combining (C.2) and (C6),

$$K = \frac{2\pi}{\rho_w^2}\sqrt{\frac{\psi_w^3}{1-\psi_w}}\left(\frac{1-\rho_w}{\rho_w}\sqrt{\frac{\psi_w}{1-\psi_w}} + 2\tan^{-1}\sqrt{\frac{\psi_w}{1-\psi_w}}\right)^{-3}. \tag{C.9}$$

The ψ_w is a constant according to (C.3) while ρ_w depends on the sliding parameter. Specifically, we can use (C.6) and (C.7) to show

$$\mathscr{S}\frac{\psi_w}{\rho_w} = \left(-\frac{2+\nu}{3} - \frac{\nu-1}{6}\rho_o^3 + \frac{1+\nu}{2}\rho_o\right)\left(\frac{1-\rho_w}{\rho_w}\sqrt{\frac{\psi_w}{1-\psi_w}} + 2\tan^{-1}\sqrt{\frac{\psi_w}{1-\psi_w}}\right)^2, \tag{C.10}$$

as well as (C.7) and (C.8) to have

$$\nu + \ln\rho_w + \frac{1-\rho_w}{2\rho_w(1-\psi_w)} - \frac{(1-\nu^2)(\rho_o+2)(\rho_o-1)^2}{(1-\nu)\rho_o^3 + 3(1+\nu)\rho_o - 2(2+\nu)} = 0 \tag{C.11}$$

Appendix D. Analytical solution to Case III

The conclusions regarding the suspended sheet in Case II, including (C.1–6), remain the same in Case III. The main difference lies in the supported sheet due to the buckle delamination. Particularly, in the buckled part, the tension in (3.29) can be solved

$$\widetilde{N}_\rho = \frac{T}{2}\left(\rho_b^2\rho^{-1} + \widetilde{\rho}^2\rho^{-1} - \rho\right), \tag{D.1}$$

where the continuity at the outer edge of the buckled zone dictates

$$\widetilde{\rho}^2 = \left[-2(2+\nu)\rho_b^2 + (1-\nu)\rho_o^3\rho_b^{-1} + 3(1+\nu)\rho_o\rho_b\right]/3. \tag{D.2}$$

As a result, equations (C.7) and (C.10) are modified to be

$$2\psi_w = AT\rho_w\left(\rho_b^2 + \widetilde{\rho}^2 - 1\right) \tag{D.3}$$

and

$$\frac{2\mathscr{S}\psi_w}{\rho_w} = \left(\rho_b^2 + \widetilde{\rho}^2 - 1\right)\left(\frac{1-\rho_w}{\rho_w}\sqrt{\frac{\psi_w}{1-\psi_w}} + 2\tan^{-1}\sqrt{\frac{\psi_w}{1-\psi_w}}\right)^2, \tag{D.4}$$

respectively. Another change stems from the displacement condition that is now defined by (3.31), namely

$$\begin{aligned}
12\frac{\psi_w}{\rho_w}(\nu + \ln\rho_w) + \frac{6\psi_w(1-\rho_w)}{\rho_w^2(1-\psi_w)} \\
= 2AT(1-\nu^2)(\rho_b-\rho_o)^2(2+\rho_o\rho_b^{-1}) + 6AT(\rho_b^2+\widetilde{\rho}^2)\ln\rho_b - 3AT(\rho_b^2-1)
\end{aligned} \tag{D.5}$$

A new version of (C.11) can be obtained by combining (D3) and (D.5),

$$3\left(\rho_b^2 + \widetilde{\rho}^2 - 1\right)\left[2(\nu + \ln\rho_w) + \left(\rho_w^{-1} - 1\right)/(1 - \psi_w)\right]$$
$$= 2\left(1 - \nu^2\right)(\rho_b - \rho_o)^2\left(2 + \rho_o\rho_b^{-1}\right) + 6\left(\rho_b^2 + \widetilde{\rho}^2\right)\ln\rho_b - 3\left(\rho_b^2 - 1\right) \qquad (D.6)$$

In Case III, therefore, the effective stiffness is still characterized by (C.9), but ρ_w and ρ_o are determined by (D.4) and (D.6), where the $\rho_o - \rho_b$ relation follows (3.27) and $\mathscr{S}$ is the only controlling parameter.

References

Akinwande, D., Brennan, C.J., Bunch, J.S., Egberts, P., Felts, J.R., Gao, H., Huang, R., Kim, J.-S., Li, T., Li, Y., Liechti, K.M., Lu, N., Park, H.S., Reed, E.J., Wang, P., Yakobson, B.I., Zhang, T., Zhang, Y.-W., Zhou, Y., Zhu, Y., 2017. A review on mechanics and mechanical properties of 2D materials—Graphene and beyond. Extreme Mech. Lett. 13, 42–77.

Androulidakis, C., Zhang, K., Robertson, M., Tawfick, S.H., 2018. Tailoring the mechanical properties of 2D materials and heterostructures. 2D Mater 5, 032005.

Beams, J.W., 1959. Mechanical properties of thin films of gold and silver. In: Neugebauer, C.A., Newkirk, J.B., Vermilyea, D.A. (Eds.), Structure and Properties of Thin Films. John Wiley and Sons, New York, p. 183, 1959.

Bertolazzi, S., Brivio, J., Kis, A., 2011. Stretching and breaking of ultrathin MoS2. ACS Nano 5, 9703–9709.

Blees, M.K., Barnard, A.W., Rose, P.A., Roberts, S.P., McGill, K.L., Huang, P.Y., Ruyack, A.R., Kevek, J.W., Kobrin, B., Muller, D.A., 2015. Graphene kirigami. Nature 524, 204.

Cao, Z., Tao, L., Akinwande, D., Huang, R., Liechti, K.M., 2015. Mixed-Mode Interactions between Graphene and Substrates by Blister Tests. J. Appl. Mech. 82, 081008.

Cao, Z., Tao, L., Akinwande, D., Huang, R., Liechti, K.M., 2016. Mixed-mode traction-separation relations between graphene and copper by blister tests. Int. J. Solids Struct. 84, 147–159.

Chandler, T.G., Vella, D., 2020. Indentation of two-dimensional solids: The signatures of geometrical and material nonlinearity. J. Mech. Phys. Solids 144, 104109.

Chen, K., 2020. A general and unified theory of the kinematic relationships in bulge tests. J. Mech. Phys. Solids 143, 104086.

Chen, K., Scales, M., Kyriakides, S., 2018. Material hardening of a high ductility aluminum alloy from a bulge test. Int. J. Mech. Sci. 138, 476–488.

Chopin, J., Vella, D., Boudaoud, A., 2008. The liquid blister test. Proc. Math. Phys. Eng. Sci. 2887–2906.

Dai, Z., Hou, Y., Sanchez, D.A., Wang, G., Brennan, C.J., Zhang, Z., Liu, L., Lu, N., 2018. Interface-Governed Deformation of Nanobubbles and Nanotents Formed by Two-Dimensional Materials. Phys. Rev. Lett. 121, 266101.

Dai, Z., Lu, N., Liechti, K.M., Huang, R., 2020a. Mechanics at the interfaces of 2D materials: Challenges and opportunities. Curr. Opin. Solid State Mater. Sci. 24, 100837.

Dai, Z., Sanchez, D.A., Brennan, C.J., Lu, N., 2020b. Radial buckle delamination around 2D material tents. J. Mech. Phys. Solids 137, 103843.

Dai, Z., Wang, G., Liu, L., Hou, Y., Wei, Y., Zhang, Z., 2016. Mechanical behavior and properties of hydrogen bonded graphene/polymer nano-interfaces. Compos Sci Technol 136, 1–9.

Dai, Z., Wang, G., Zheng, Z., Wang, Y., Zhang, S., Qi, X., Tan, P., Liu, L., Xu, Z., Li, Q., Cheng, Z., Zhang, Z., 2019. Mechanical responses of boron-doped monolayer graphene. Carbon 147, 594–601.

Davidovitch, B., Guinea, F., 2020. Indentation of solid membranes on rigid substrates with Van-der-Waals attraction. arXiv preprint arXiv:2008.01199.

Davidovitch, B., Schroll, R.D., Vella, D., Adda-Bedia, M., Cerda, E.A., 2011. Prototypical model for tensional wrinkling in thin sheets. Proc. Natl. Acad. Sci. USA 108, 18227–18232.

Davidovitch, B., Sun, Y., Grason, G.M., 2019. Geometrically incompatible confinement of solids. Proc. Natl. Acad. Sci. USA 116, 1483–1488.

Davidovitch, B., Vella, D., 2018. Partial wetting of thin solid sheets under tension. Soft Matter 14, 4913–4934.

Diab, M., Kumaraswamy, N., Reece, G.P., Hanson, S.E., Fingeret, M.C., Markey, M.K., Ravi-Chandar, K., 2020. Characterization of human female breast and abdominal skin elasticity using a bulge test. J. Mech. Behav. Biomed 103, 103604.

Falin, A., Cai, Q., Santos, E.J., Scullion, D., Qian, D., Zhang, R., Yang, Z., Huang, S., Watanabe, K., Taniguchi, T., 2017. Mechanical properties of atomically thin boron nitride and the role of interlayer interactions. Nat. Commun. 8 ncomms15815.

Gong, L., Kinloch, I.A., Young, R.J., Riaz, I., Jalil, R., Novoselov, K.S., 2010. Interfacial stress transfer in a graphene monolayer nanocomposite. Adv. Mater. 22, 2694–2697.

Han, E., Yu, J., Annevelink, E., Son, J., Kang, D.A., Watanabe, K., Taniguchi, T., Ertekin, E., Huang, P.Y., van der Zande, A.M., 2020. Ultrasoft slip-mediated bending in few-layer graphene. Nat. Mater. 19, 305–309.

Hencky, H., 1915. On the stress state in circular plates with vanishing bending stiffness. Z. Math. Phys. 63, 311–317.

Hod, O., Meyer, E., Zheng, Q., Urbakh, M., 2018. Structural superlubricity and ultralow friction across the length scales. Nature 563, 485–492.

Itozaki, H., 1982. Mechanical properties of composition modulated copper-palladium foils. Northwestern University, Evanston, IL.

Janssens, S., Sutisna, B., Giussani, A., Kwiecinski, J., Vázquez-Cortés, D., Fried, E., 2020. Boundary curvature effect on the wrinkling of thin suspended films. Appl. Phys. Lett. 116, 193702.

Jia, F., Amar, M.B., 2020. Scaling laws and snap-through events in indentation of perforated membranes. J. Mech. Phys. Solids 135, 103797.

Jiang, T., Huang, R., Zhu, Y., 2014. Interfacial Sliding and Buckling of Monolayer Graphene on a Stretchable Substrate. Adv. Funct. Mater. 24, 396–402.

Jiang, Y., Mao, J., Duan, J., Lai, X., Watanabe, K., Taniguchi, T., Andrei, E.Y., 2017. Visualizing Strain-Induced Pseudomagnetic Fields in Graphene through an hBN Magnifying Glass. Nano Lett 17, 2839–2843.

King, H., Schroll, R.D., Davidovitch, B., Menon, N., 2012. Elastic sheet on a liquid drop reveals wrinkling and crumpling as distinct symmetry-breaking instabilities. Proc. Natl. Acad. Sci. USA 109, 9716–9720.

Kitt, A.L., Qi, Z., Rémi, S., Park, H.S., Swan, A.K., Goldberg, B.B., 2013. How graphene slides: Measurement and theory of strain-dependent frictional forces between graphene and SiO2. Nano Lett 13, 2605–2610.

Koenig, S.P., Boddeti, N.G., Dunn, M.L., Bunch, J.S., 2011. Ultrastrong adhesion of graphene membranes. Nat. Nanotechnol. 6, 543–546.

Komaragiri, U., Begley, M., Simmonds, J., 2005. The mechanical response of freestanding circular elastic films under point and pressure loads. J. Appl. Mech. 72, 203–212.

Kudin, K.N., Scuseria, G.E., Yakobson, B.I., 2001. C 2 F, BN, and C nanoshell elasticity from ab initio computations. Phys. Rev. B 64, 235406.

Kumar, H., Dong, L., Shenoy, V.B., 2016. Limits of Coherency and Strain Transfer in Flexible 2D van der Waals Heterostructures: Formation of Strain Solitons and Interlayer Debonding. Sci. Rep. 6, 21516.

Kumar, H., Er, D., Dong, L., Li, J., Shenoy, V.B., 2015. Elastic Deformations in 2D van der waals Heterostructures and their Impact on Optoelectronic Properties: Predictions from a. Multiscale Computational Approach. Sci. Rep. 5, 10872.

Lee, C., Wei, X., Kysar, J.W., Hone, J., 2008. Measurement of the elastic properties and intrinsic strength of monolayer graphene. Science 321, 385–388.

Lipatov, A., Lu, H., Alhabeb, M., Anasori, B., Gruverman, A., Gogotsi, Y., Sinitskii, A., 2018. Elastic properties of 2D Ti3C2Tx MXene monolayers and bilayers. Sci. Adv. 4, eaat0491.

Liu, K., Yan, Q., Chen, M., Fan, W., Sun, Y., Suh, J., Fu, D., Lee, S., Zhou, J., Tongay, S., 2014. Elastic properties of chemical-vapor-deposited monolayer MoS2, WS2, and their bilayer heterostructures. Nano Lett 14, 5097–5103.

López-Polín, G., Gómez-Navarro, C., Parente, V., Guinea, F., Katsnelson, M.I., Pérez-Murano, F., Gómez-Herrero, J., 2015. Increasing the elastic modulus of graphene by controlled defect creation. Nat. Phys. 11, 26–31.

Luo, H., Li, X., Zhao, Y., Yang, R., Hao, Y., Gao, Y.-n., Shi, N.N., Guo, Y., Liu, G., Zhao, L., 2020. Simultaneous Generation of Direct-and Indirect-Gap Photoluminescence in Multilayer MoS2 Bubbles. arXiv preprint arXiv:2002.05344.

Mansfield, E.H., 2005. The Bending and Stretching of Plates. Cambridge University Press.

Novoselov, K.S., Mishchenko, A., Carvalho, A., Castro Neto, A.H., 2016. 2D materials and van der Waals heterostructures. Science 353, aac9439.

Reserbat-Plantey, A., Kalita, D., Han, Z., Ferlazzo, L., Autier-Laurent, S., Komatsu, K., Li, C., Weil, R., Ralko, A., Marty, L., Gueron, S., Bendiab, N., Bouchiat, H., Bouchiat, V., 2014. Strain superlattices and macroscale suspension of graphene induced by corrugated substrates. Nano Lett 14, 5044–5051.

Schwerin, E., 1929. Über Spannungen und Formänderungen kreisringförmiger Membranen. ZAMM-Journal of Applied Mathematics and Mechanics/Zeitschrift für Angewandte Mathematik und Mechanik 9, 482–483.

Small, M.K., Nix, W., 1992. Analysis of the accuracy of the bulge test in determining the mechanical properties of thin films. J. Mater. Res 7, 1553–1563.

Tu, Q., Spanopoulos, I., Yasaei, P., Stoumpos, C.C., Kanatzidis, M.G., Shekhawat, G.S., Dravid, V.P., 2018. Stretching and Breaking of Ultrathin 2D Hybrid Organic-Inorganic Perovskites. ACS Nano 12, 10347–10354.

Vella, D., 2019. Buffering by buckling as a route for elastic deformation. Nat. Rev. Phys. 1, 425–436.

Vella, D., Davidovitch, B., 2017. Indentation metrology of clamped, ultra-thin elastic sheets. Soft Matter 13, 2264–2278.

Vella, D., Davidovitch, B., 2018. Regimes of wrinkling in an indented floating elastic sheet. Phys Rev E 98, 013003.

Vlassak, J., 1994. New experimental techniques and analysis methods for the study of mechanical properties of materials in small volumes. Stanford University, Stanford, CA.

Vlassak, J., Nix, W., 1992. A new bulge test technique for the determination of Young's modulus and Poisson's ratio of thin films. J. Mater. Res. 7, 3242–3249.

Wang, G., Dai, Z., Wang, Y., Tan, P., Liu, L., Xu, Z., Wei, Y., Huang, R., Zhang, Z., 2017. Measuring Interlayer Shear Stress in Bilayer Graphene. Phys. Rev. Lett. 119, 036101.

Wang, G., Dai, Z., Xiao, J., Feng, S., Weng, C., Liu, L., Xu, Z., Huang, R., Zhang, Z., 2019. Bending of Multilayer van der Waals Materials. Phys. Rev. Lett. 123, 116101.

Wei, X., Fragneaud, B., Marianetti, C.A., Kysar, J.W., 2009. Nonlinear elastic behavior of graphene: Ab initio calculations to continuum description. Phys. Rev. B 80, 205407.

Xu, J., Yuan, G., Zhu, Q., Wang, J., Tang, S., Gao, L., 2018. Enhancing the Strength of Graphene by a Denser Grain Boundary. ACS Nano 12, 4529–4535.

Yu, J., Kim, S., Ertekin, E., van der Zande, A.M., 2020. Material-Dependent Evolution of Mechanical Folding Instabilities in Two-Dimensional Atomic Membranes. ACS Appl. Mater. Interfaces 12, 10801–10808.

Zhang, D.B., Akatyeva, E., Dumitrica, T., 2011. Bending ultrathin graphene at the margins of continuum mechanics. Phys. Rev. Lett. 106, 255503.